

Optimization under turbulence model uncertainty for aerospace design

L.W. Cook,¹ A.A. Mishra,^{2, a)} J.P. Jarrett,³ K.E. Willcox,⁴ and G. Iaccarino⁵

¹⁾*Massachusetts Institute of Technology, Cambridge, MA, 02139,*

USA.

²⁾*Center for Turbulence Research, Stanford University, Stanford, CA-94305,*

USA

³⁾*Department of Engineering, University of Cambridge, Cambridge, CB2 1PZ,*

United Kingdom

⁴⁾*Oden Institute for Computational Engineering and Sciences,*

University of Texas at Austin, TX, 78712, USA.

⁵⁾*Center for Turbulence Research, Stanford University, Stanford, CA-94305,*

USA.

(Dated: 28 October 2019)

The computational economy of Reynolds-Averaged Navier Stokes solvers encourages their widespread use in the optimization of aerospace designs. Unfortunately the real-world performance of the resulting optimized designs may have shortcomings. A common contributor to this shortfall is a lack of adequately accounting for the uncertainty introduced by the structure of the turbulence model. We investigate whether including measures of turbulence-based uncertainty, as predicted by the eigenspace perturbation method, in an optimization under uncertainty framework can result in designs that are more robust with respect to turbulence model-form uncertainty. In an asymmetric diffuser design problem and a transonic airfoil design problem, our optimization formulation taking account of turbulence-based uncertainty obtained designs that were more robust to turbulence model uncertainty than optimal designs obtained via deterministic approaches.

^{a)}Electronic mail: aashwin@stanford.edu

I. INTRODUCTION

With the increase in computational resources that has become accessible in recent decades, aerospace design is becoming increasingly a simulation-driven process¹. When simulations of an aerospace system are available, optimization can be used as a design tool to search for designs with good simulated performance measures, such as high efficiency, low weight, or low drag. However, traditional deterministic optimization can lead to designs that are non-robust with respect to uncertainties in the simulation and that see degraded performance when realized. Therefore the importance of considering the influence of uncertainty within optimization is becoming increasingly recognized^{1,2}. Optimization under uncertainty (OUU) methods have been developed to explicitly account for the influence of uncertainty on the simulated performance³.

Uncertainties in aerospace design arise from a variety of sources, including operating conditions, material and heat transfer properties, and the numerical simulations themselves. To account for the effects of turbulence, the majority of Computational Fluid Dynamics (CFD) studies used in aerospace design simulations rely on eddy-viscosity based closures, such as the $k - \epsilon$ and $k - \omega$ models. Due to assumptions and simplifications introduced in the formulation of such Reynolds Averaged Navier Stokes (RANS) models, these models are limited in the characteristics of turbulent flows that they can replicate and their overall fidelity. Such simplifications include coarse graining where it is assumed that the Reynolds stress tensor can adequately describe the turbulent flow field, the eddy viscosity hypothesis that assumes the instantaneous Reynolds stress anisotropy to be proportional to the instantaneous mean rate of strain, the application of the gradient diffusion hypothesis to model turbulent transport, the limitations in the modeled evolution equations for the turbulent dissipation, besides others. These simplifications introduce structural uncertainty in the predictions of simulations using RANS models.

For example, in turbulent flows with significant effects of mean rotation, such as swirl or strong streamline curvature, the fidelity of linear eddy-viscosity-based closures is unsatisfactory^{4,5}. In turbulent flows with flow separation and reattachment, eddy-viscosity-based models have had limited success^{6,7}. Furthermore, in relatively simpler flows such as turbulent flows in ducts, isotropic eddy-viscosity-based models are not able to reproduce the secondary flows that develop near the corners of the domain⁸.

The use of simulations based on such turbulence models leads to imprecise measures of the performance. The designs resulting from optimizing these imprecise measures of performance

can depend on the particular turbulence model used, and are likely to be sub-optimal in reality^{9–12}. However, design optimization under turbulence model-form uncertainty is an avenue that has not been investigated deeply. The key hurdles are two-fold. Firstly, it is challenging to produce accurate estimates of the uncertainty in turbulence predictions arising due to the model form. Secondly, it is not clear how such measures of turbulence uncertainty should be integrated into design optimization frameworks.

Previous work has begun to address the first hurdle, by developing methods for rigorously propagating measures of turbulence model-form uncertainty in CFD simulations. In this article, we consider the second hurdle, and investigate integrating a recently developed method for propagating turbulence model-form uncertainty into a robust optimization framework. We propose an optimization formulation and apply it to key aerospace design problems, and we examine whether this optimization formulation results in designs with higher robustness to turbulence model form uncertainty than traditional deterministic optimization methods.

II. METHODOLOGY

This section provides an overview of the methodology adopted for estimating turbulence model uncertainties and the optimization formulation that takes account of this uncertainty.

A. Eigenspace perturbations: Estimating turbulence model uncertainty

In this investigation, to estimate the uncertainty due to turbulence models we utilize the SU2 EQUiPS library¹³, based on the Eigenspace perturbation framework¹⁴. While both are discussed in detail in literature, we provide an overview for the reader.

The Reynolds stress tensor, $R_{ij} = \langle u_i u_j \rangle$, is one of the central quantities of interest for turbulence modeling. The Reynolds stress tensor can be decomposed into the anisotropic and deviatoric components as $R_{ij} = 2k(b_{ij} + \frac{\delta_{ij}}{3})$. Here, $k (= \frac{R_{ii}}{2})$ is the turbulent kinetic energy and $b_{ij} (= \frac{R_{ij}}{2k} - \frac{\delta_{ij}}{3})$ is the Reynolds stress anisotropy tensor. The Reynolds stress anisotropy tensor can be expressed as $b_{in}v_{nl} = v_{in}\Lambda_{nl}$, where v_{nl} is the matrix of orthonormal eigenvectors and Λ_{nl} is the traceless diagonal matrix of eigenvalues λ_k . Multiplication by v_{jl} yields $b_{ij} = v_{in}\Lambda_{nl}v_{jl}$. On substitution, this yields

$$R_{ij} = 2k(v_{in}\Lambda_{nl}v_{jl} + \frac{\delta_{ij}}{3}). \quad (1)$$

The tensors ν and Λ are ordered such that $\lambda_1 \geq \lambda_2 \geq \lambda_3$. To account for the errors due to closure assumptions, this eigenspace representation of the Reynolds stress tensor is perturbed. These perturbations are injected directly into the modeled Reynolds stress during the CFD solution iterations. This perturbed form is expressed as:

$$R_{ij}^* = 2k^* \left(\frac{\delta_{ij}}{3} + v_{in}^* \Lambda_{nl}^* v_{lj}^* \right) \quad (2)$$

where $*$ represents the perturbed quantities. The perturbations to the eigenvalues, Λ , correspond to varying the componentiality of the flow (or the shape of the Reynolds stress ellipsoid). Similarly, the perturbations to the eigenvectors and the turbulent kinetic energy vary the orientation and amplitude of the Reynolds stress ellipsoid. These perturbations are sequentially applied to the modeled Reynolds stress tensor.

The eigenvalue perturbation can be represented on the barycentric map¹⁵. In this representation, all realizable states of the Reynolds stress tensor lie on or inside the barycentric triangle. The vertices of this triangle represent the one, two and three component limiting states of the turbulent flow field. A linear map between the co-ordinates on this triangle \mathbf{x} and the Reynolds stress anisotropy eigenvalues λ_i is defined by

$$\mathbf{x} = \mathbf{x}_{1C}(\lambda_1 - \lambda_2) + \mathbf{x}_{2C}(2\lambda_2 - 2\lambda_3) + \mathbf{x}_{3C}(3\lambda_3 - 1). \quad (3)$$

This linear transform can be expressed as $\mathbf{x} = \mathbf{B}\boldsymbol{\lambda}$. In physical terms, this invertible, one-to-one mapping expresses any realizable state of the Reynolds stress eigenvalues as a convex combination of the three limiting states of turbulence. The projection of the eigenvalue perturbation in the barycentric map has both a direction and a magnitude. In this application, the perturbations are aligned towards the vertices of the barycentric triangle (or the limiting states of turbulence). The magnitude of the eigenvalue perturbation in the barycentric triangle is represented by $\Delta_B \in [0, 1]$. The perturbed barycentric coordinates \mathbf{x}^* are given by $\mathbf{x}^* = \mathbf{x} + \Delta_B(\mathbf{x}^t - \mathbf{x})$, where \mathbf{x}^t denotes the target vertex (representing one of the one-, two-, or three-component limiting states) and \mathbf{x} is the unperturbed model prediction. Thus, $\Delta_B = 0$ would leave the state unperturbed and $\Delta_B = 1$ would perturb any arbitrary state till the vertices of the barycentric triangle.

The eigenvector perturbations vary the alignment of the Reynolds stress ellipsoid. These are guided by the turbulence production mechanism, $\mathcal{P} = -R_{ij} \frac{\partial U_i}{\partial x_j}$. The eigenvector perturbations seek to modulate turbulence production by varying the Frobenius inner product $\langle A, R \rangle = tr(AR)$, where A is the mean velocity gradient and R is the Reynolds stress tensor. For the purposes of

bounding all permissible dynamics, we seek the extremal values of this inner product. In the coordinate system defined by the eigenvectors of the rate of strain tensor, the critical alignments

of the Reynolds stress eigenvectors are given by¹⁴ $v_{max} = \begin{bmatrix} 1 & 0 & 0 \\ 0 & 1 & 0 \\ 0 & 0 & 1 \end{bmatrix}$ and $v_{min} = \begin{bmatrix} 0 & 0 & 1 \\ 0 & 1 & 0 \\ 1 & 0 & 0 \end{bmatrix}$. The range of this inner product is $[\lambda_1 \gamma_3 + \lambda_2 \gamma_2 + \lambda_3 \gamma_1, \lambda_1 \gamma_1 + \lambda_2 \gamma_2 + \lambda_3 \gamma_3]$, where $\gamma_1 \geq \gamma_2 \geq \gamma_3$ are the eigenvalues of the symmetric component of A .

This eigenspace perturbation framework gives us 5 distinct extremal states of the Reynolds stress tensor. These correspond to 3 extremal states of the componentiality ($1C, 2C, 3C$) and 2 extremal alignments of the Reynolds stress eigenvectors, (v_{min}, v_{max}) . For the $3C$ limiting state, due to rotational symmetry, eigenvector perturbations are superfluous.

Finally, we outline how the uncertainty estimates are given from this set of perturbed CFD simulations. This process is schematically exhibited in Fig. 1. The illustrative flow used is the canonical case of separated turbulent flow in a planar diffuser. The conditions and the experimental data are from the experimental study of Buice & Eaton¹⁶.

The central panel of Fig. 1 outlines the unperturbed, baseline CFD solution. Using the $k - \omega$ Shear Stress Transport (SST) model, this leads to a unique flow field realization in the flow domain. To illustrate the composition of the uncertainty bounds, we choose a specific location in the domain, specifically at $x/H = 24$ which is marked in the figures. This unique flow field realization from the SST model leads to a singleton profile for the mean velocity, u_i/u , shown in panel C with the solid gray line.

The upper and lower panels of the figure outline perturbed solutions. While there are 5 perturbed states as discussed in the last subsection, we exhibit only 2 of these in the schematic illustration. Each of these perturbed solutions leads to a different realization of the flow field, as is illustrated in panel B. These flow realizations differ in essential aspects. For instance, the perturbation to the state $(1C, v_{max})$ maximizes the turbulence production mechanism and thus, suppresses flow separation. The perturbation to the state $(3C, v_{min})$ minimizes the turbulence production mechanism and thus, strengthens flow separation. This is evidenced in the variation of the separation zones in panel B. Each of these perturbations leads to a different flow field and consequently, the velocity profiles from these flow fields are different as well. The velocity profiles at $x/H = 24$ from the $(1C, v_{max})$ and $(3C, v_{min})$ are shown in panel C with the dashed and dot-dashed lines respectively (panel C also shows the profiles from the $(1C, v_{min})$, $(2C, v_{max})$ and $(2C, v_{min})$)

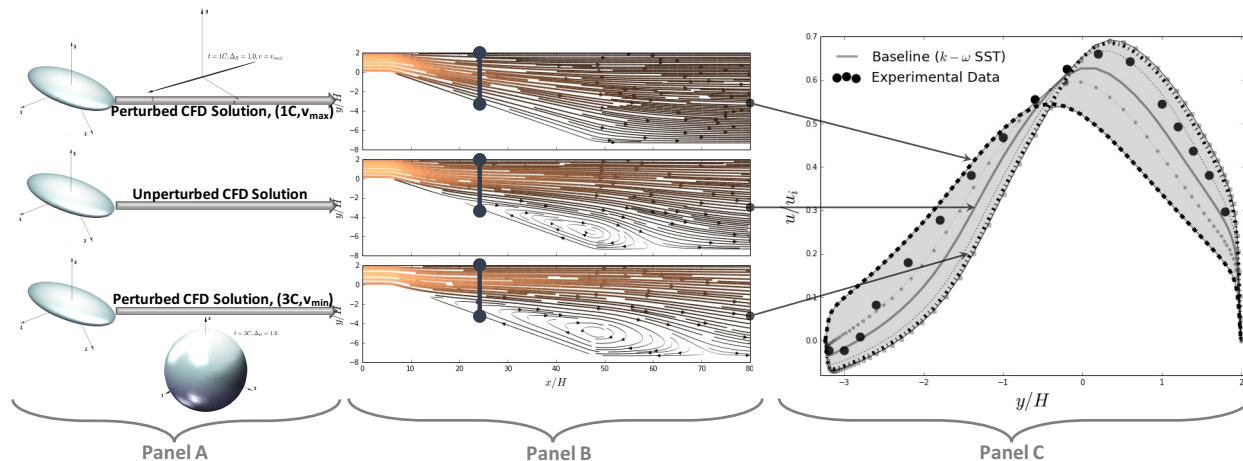


FIG. 1: Schematic outlining the stages in the computation of uncertainty estimates. *Panel A*: RANS Simulations with varied perturbations; *Panel B*: Varied perturbed realizations of turbulent flow fields; *Panel C*: Compositions of uncertainty estimates from union of perturbed profiles of QoIs.

perturbations using the dotted line, dotted line with circles and dotted lines with squares). The uncertainty estimates on the profiles of a quantity of interest (QoI) at a location are given by the union of all the states lying in the profiles from this set of perturbed RANS simulations. This is illustrated by the gray shaded zone in Fig. 1 panel C.

The uncertainty estimates do not define a probability distribution on the possible realizations from the turbulence model. The results presented should be interpreted as the range of possible flow evolution corresponding to the turbulence model, but the likelihood of different sub-sections of this range is not quantified.

Finally, we acknowledge some limitations of this uncertainty estimation methodology. The errors and uncertainties in turbulence models are not uniform across the computational domain. These are higher in regions where the assumptions and simplifications made during model formulation are invalid. For instance, eddy-viscosity models will exhibit higher errors in regions with flow separation, significant streamline curvature, rotational effects, etc. The perturbations are intended to account for such limitations in the turbulence models. However, the perturbations are uniformly applied to the entire domain. Thus, the uncertainty estimates from this procedure may be conservative in regions of the flow domain where the turbulence model predictions are satisfactory.

B. Optimization Under Uncertainty

Optimization is the process of determining values of design variables that lead to the minimization (or maximization) of an objective function, subject to constraints. Mathematically, this can be expressed as:

$$\begin{aligned} \text{Minimize} \quad & f(\mathbf{x}), \\ \text{Subject to} \quad & \mathbf{g}(\mathbf{x}) \leq 0. \end{aligned} \tag{4}$$

Here, the vector \mathbf{x} represents the design variables; $f(\mathbf{x})$ is the objective function to be minimized; $\mathbf{g}(\mathbf{x})$ represents a vector of constraint functions. When used for design, optimization is a procedure for exploring the design space in order to improve performance measures of designs. When simulations of the performance measures are subject to uncertainty, ignoring the effects of these uncertainties in an optimization can give rise to designs that are optimal according to the simulation but give degraded performance when realized¹. Therefore the importance of taking account of such uncertainties in an optimization under uncertainty framework when using optimization for design problems is becoming increasingly recognized.

In optimization under uncertainty (OUU), the objective function is a measure of performance under uncertainty. Common OUU frameworks include robust design¹⁷, where designs insensitive to small changes in the uncertain quantities are sought, and reliability-based design¹⁸ where designs with a small probability of failure are sought.

In this paper, we consider specifically turbulence-based uncertainty, and the eigenspace perturbation method for measuring the effect of this uncertainty. As discussed in section II A, this method results in a set of possible values for every quantity of interest, corresponding to the predictions from the perturbed RANS simulations. As illustrated on Fig. 1, the envelope of these values provides an estimate for the bounds in which the true solution should lie. On Fig. 1, the envelope of the five solutions gives an interval for velocity at a given location. This same enveloping approach is used to obtain intervals (i.e. bounds on the value) for the performance metrics that would be used as objectives or constraints in a deterministic optimization. This measure of uncertainty is not probabilistic, meaning standard probabilistic robust optimization formulations are not appropriate.

The key question is therefore how this measure of uncertainty should be used in an OUU formulation, in order to obtain designs that are insensitive to turbulence model-form uncertainties and so that should achieve good performance in reality (a robust optimization). One approach would

be to *explicitly* optimize for designs with a small interval of performance under the eigenspace perturbations (for example by penalizing large performance intervals in the objective function). However, explicitly optimizing for robustness can often lead to designs that are robust but that exhibit consistently poor performance¹⁹.

We anticipate that by optimizing the worst case performance over the perturbed solutions, we will obtain a design that is also robust with respect to turbulence model-form uncertainty, without explicitly including a robustness term in the optimization. Therefore in this paper, we use the worst case of the perturbed solutions as our objective function. Mathematically, our approach can be expressed as:

$$\begin{aligned} \text{Minimize} \quad & \max\{f_i(\mathbf{x}) \mid i = 1, \dots, 5\}, \\ \text{Subject to} \quad & g(\mathbf{x}) \leq 0, \end{aligned} \tag{5}$$

where f_i is the objective function according to the i^{th} perturbed solution (out of the five used in the eigenspace perturbation framework), and $\max\{f_i(\mathbf{x}) \mid i = 1, \dots, 5\}$ is the largest of these objective function values.

With reference to prior studies into robust optimization, our approach is similar in principle to the pessimistic robust optimization approach^{20,21}. This is sometimes known as the robust counterpart²² (particularly in the context of ensuring constraint satisfaction) or robust regularization²³.

We investigate whether this formulation can give rise to designs that are more robust with respect to the structural uncertainties in turbulence models than deterministic approaches, whilst still obtaining good performance.

III. APPLICATION & RESULTS

We perform studies in two key aerospace applications. The goal is to investigate whether optimizing the worst case of the envelope due to eigenspace perturbations obtains a design that is more robust as compared to the designs obtained via the deterministic design paradigm. If so, it indicates a traditional CFD-based optimization in these applications is likely to give designs that are sensitive to the structural uncertainties in turbulence models, and that improved results can be obtained by accounting for turbulence model-form uncertainty within the optimization.

For each of the design problems investigated, we commence with an outline of the design problem, discuss the specific limitations of RANS models encountered, and highlight the errors

and uncertainties introduced due to RANS model form. Thence, we provide an in depth overview of the computational details of the simulations, and carry out requisite mesh independence as well as validation studies. This is followed by performing both a traditional deterministic design optimization, and an optimization under uncertainty using the eigenspace perturbation method. The designs resulting from the two optimization formulations are compared, and the physics and modeling rationale underlying their differences are discussed.

In this investigation, we focus on the two-equation $k - \omega$ SST model²⁴ and the Spalart-Allmaras turbulence model²⁵, as archetypal examples of turbulence models used in design. The $k - \omega$ SST model is one of the more accurate eddy-viscosity based closures and represents the workhorse for engineering design studies. The Spalart-Allmaras turbulence model provides accurate predictions for aerospace flows and is widely used in aerospace design studies.

1. Notation

In the results, we outline the predictions from all the individual perturbed simulations of the eigenspace perturbation method for comparison. These are reported, along with their nomenclature, in Figure 2. Figure 2 exhibits the state of the Reynolds stress ellipsoid for each of the perturbed states, starting from an arbitrary initial state. The following labels are used: p0 means eigenvectors permuted for minimum production, p1 means eigenvectors permuted for maximum production, c1, c2, c3 correspond to eigenvalues perturbed to give 1-component, 2-component and 3-component anisotropy respectively. In the figure, the exact orientation and magnitude of all the five perturbed states are outlined.

Note that a priori, it can't be predicted that a specific perturbed simulation will lead to the minimum value of the objective function. Similarly, the type of perturbation leading to the minimum value of the objective function may change during the optimization design iterations.

A. Asymmetric Diffuser

Diffusers are commonplace in aircraft and jet engines, for instance to compress the air flow ahead of turbine engine combustors and to slow the air intake to the compressor. Features of the flow such as separation over a smooth wall, reattachment and redevelopment of the downstream boundary layer offer challenges to eddy-viscosity based models^{26,27}. This is exacerbated by the

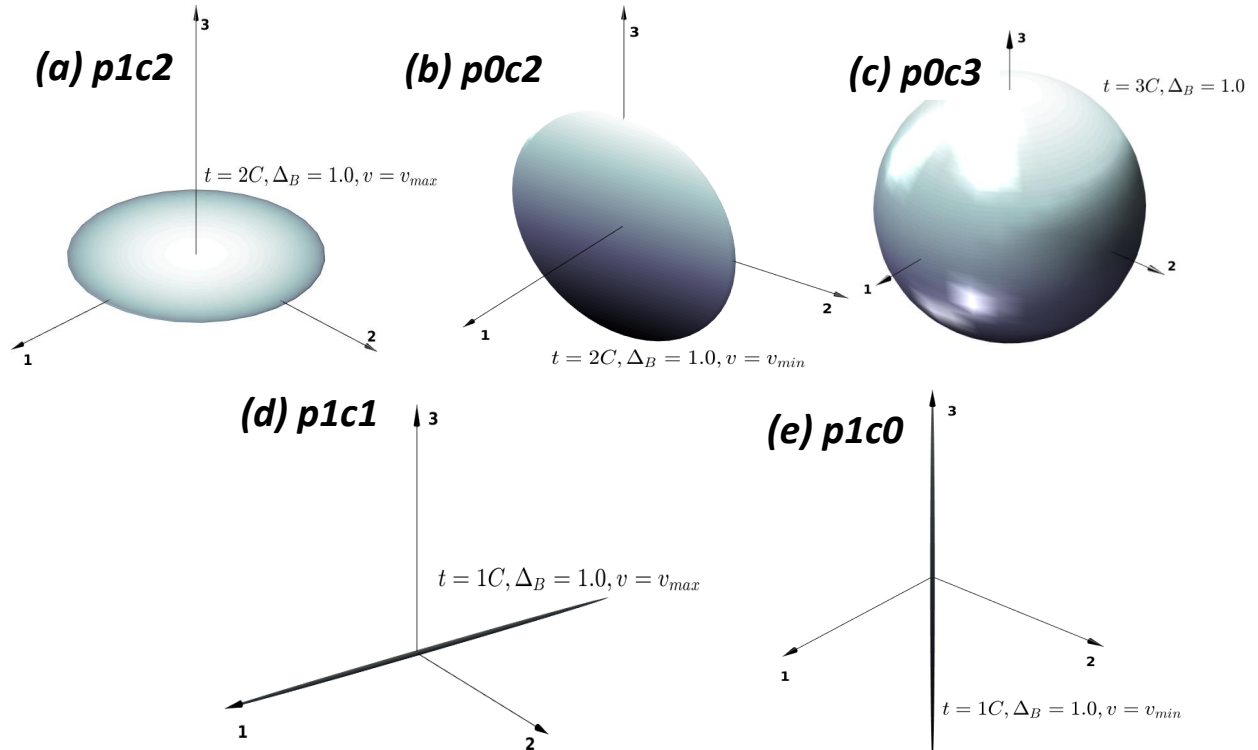


FIG. 2: Schematic outlining the different perturbations and their nomenclature.

inability of eddy-viscosity models to account for the Reynolds stress anisotropy governing the secondary currents in the inflow duct^{6,7}. Using such turbulence models for deterministic design optimization, leads to designs that are dependent upon the choice of the model as is reported in Lim and Choi¹¹.

We investigate the design of a two-dimensional, asymmetric diffuser, starting with a baseline geometry reproduced from Buice and Eaton¹⁶, which gives experimental results for this geometry. The diffuser operates with an inlet bulk velocity $U_b \simeq 19.8$, which is the density averaged velocity in the channel, and which for incompressible flow is given by:

$$U_b = \frac{\int u(y)dy}{h}, \quad (6)$$

where $u(y)$ is the x-velocity at height y , and h is the channel width. For the baseline diffuser, the Reynolds number based on this bulk velocity and the inlet channel is $\simeq 1.8 \times 10^4$.

The objective function we are designing for is pressure recovery, which is the difference be-

tween the velocity-averaged pressure at the outlet and the inlet, normalized by the inlet dynamic pressure:

$$PR = \frac{\frac{1}{U_{b,in}h_{in}} \int_{\Gamma_{out}} u(y)p(y)dy - \frac{1}{U_{b,out}h_{out}} \int_{\Gamma_{out}} u(y)p(y)dy}{0.5\rho U_{b,in}^2} \quad (7)$$

where Γ_{in} is the inlet plane, h_{in} is the inlet plane height, Γ_{out} is the out plane, h_{out} is the outlet plane height, $p(y)$ is static pressure, $u(y)$ is x-velocity, and ρ is density. This measure is often used in turbomachinery applications as an indicator for the performance of the diffuser designs²⁸.

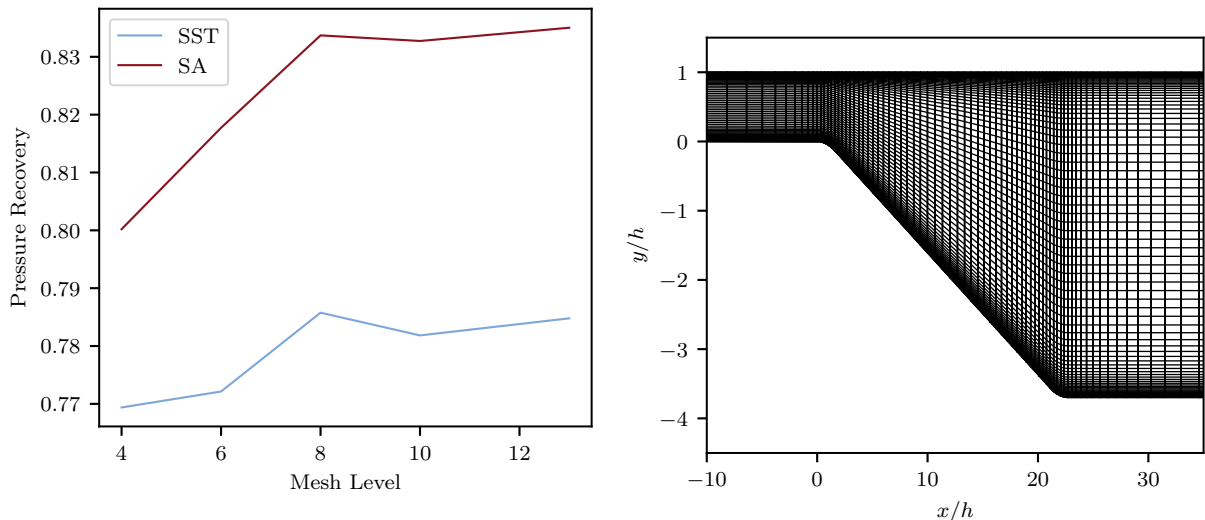
1. Computational Setup

For this investigation, we use an automated mesh generation that takes in the diffuser length, output channel width, radius of both corners of the diffuser ramp, and 5 free form deformation (FFD) parameters that modify the ramp surface, and generates a structured mesh at a given fidelity level. Free form deformation treats the surface as a bezier curve, and deforms it by moving the control points for the bezier curve²⁹. The mesh extends to $100h$ upstream of the diffuser and to $56h$ downstream of the diffuser, which corresponds to an adequate extent upstream to ensure fully developed channel flow at the inlet plane. Following best practice guidelines³⁰, regardless of the turbulence model being used, the solver is initially run with the Spalart-Allmaras turbulence model²⁵ until a reasonable convergence level, as this provides a useful restart solution for the solver that better predicts the boundary layer development. The boundary conditions are a uniform inlet velocity equal to 19.8m/s, given by a mass flow inlet condition with a constant density, and the outlet static pressure is set to 101240 bar.

In both applications, we use the SU2 open source solver, and using a 2nd order scheme, a Roe convective numerical method with a slope limiter for the flow, a scalar upwind scheme for the turbulence equations, and an implicit time discretization. The solver is run until a Cauchy convergence criteria of 5×10^{-5} on the lift coefficient is met. The flow is treated as compressible.

2. Validation

Here we validate the mesh and the computational setup, for two different turbulence models: the one-equation SA model²⁵, and the two-equation $k - \omega$ SST model²⁴. First we generate meshes for the baseline diffuser geometry at different fidelity levels and look at the pressure recovery for the two turbulence models, and plot the results in Figure 3. We determine that fidelity level 8 is



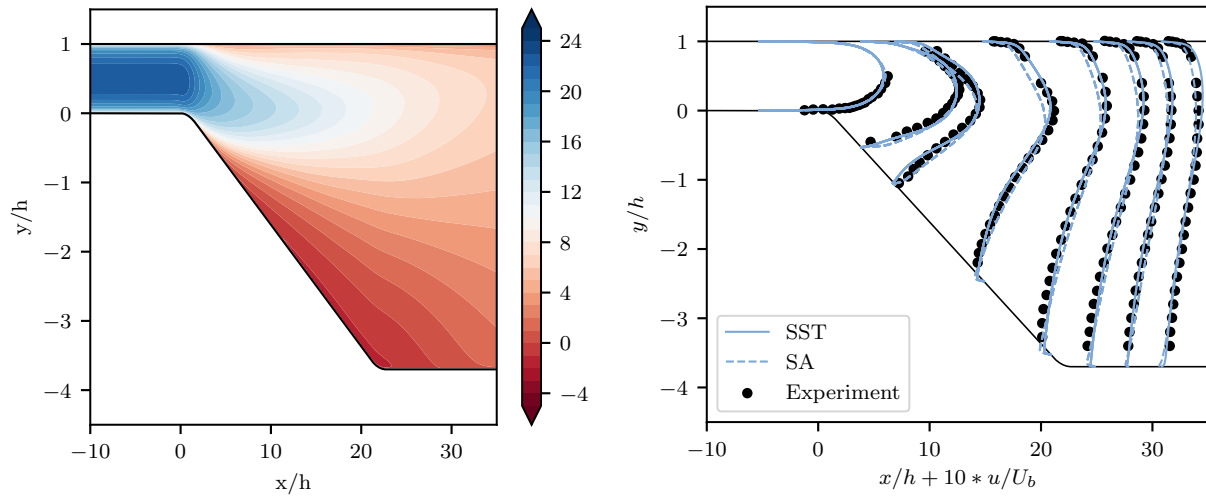
(a) Convergence of pressure recovery with mesh fidelity

(b) Fidelity 8 Mesh (every 4th vertical line shown)

FIG. 3: Validation for the two-dimensional (2D) diffuser computational setup, compared to experimental results from Buice and Eaton¹⁶: (a) Pressure recovery, (b) Final mesh fidelity.

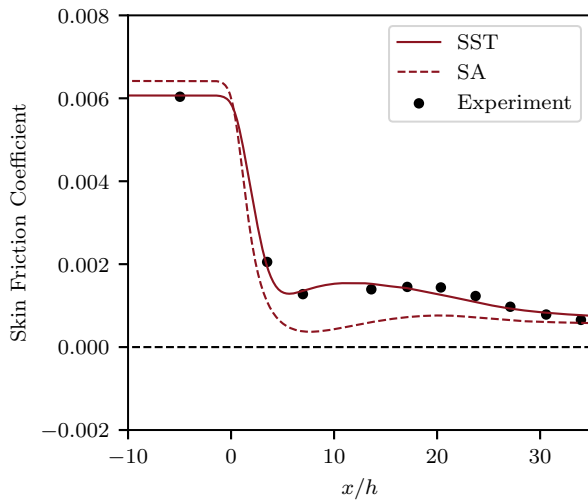
a suitably fine mesh, which corresponds to 24395 elements, and $y^+ \simeq 0.6$ on the lower surface at the inlet to the diffuser. In figure 4 we compare the flow given by this mesh with experimental results. These results are in agreement with prior numerical investigations³⁰, and we can see that the SST model predicts the skin friction with higher accuracy, especially on the upper surface of the diffuser, and gives more accurate velocity profiles than the SA model on Figure 4b. On Figure 4d we can see that both turbulence models over predict the amount of separation on the lower surface. The length of the separation bubble is overpredicted by the models by over 15%. This is in agreement with prior studies of this case^{6,7}. At this juncture, this computational setup is considered satisfactory to perform optimization studies.

Lim and Choi¹¹ perform a number of optimization studies on this diffuser case, with different constraints on the length and width of the diffuser geometry. Many of the optimal designs in Lim and Choi¹¹ get very close to having zero friction along the diffuser ramp surface, suggesting that the optimum shape would be sensitive to the accuracy of this skin friction, and hence the choice of the turbulence model. This makes it an attractive optimization case to test the effect of the choice of turbulence model upon the final optimized design. Along with the results of the previous study by¹¹, the difference in predictions between the SA and SST models highlights the turbulence

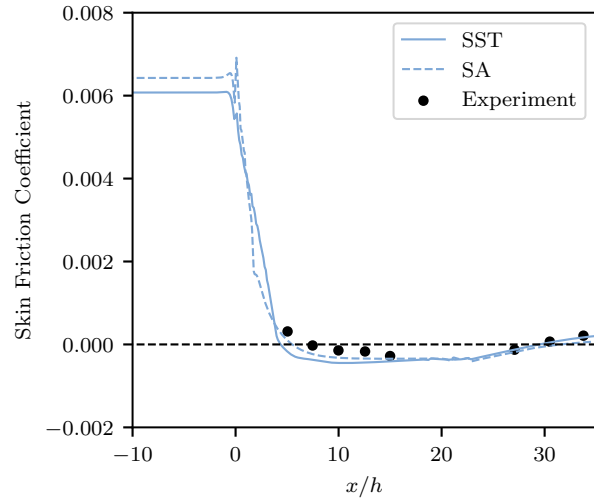


(a) X-Velocity of baseline diffuser

(b) X-Velocity comparison



(c) Upper surface skin friction comparison



(d) Lower surface skin friction comparison

FIG. 4: Validation for the 2D diffuser computational setup, compared to experimental results from Buice and Eaton¹⁶: (a) Baseline velocity contours using the $k - \omega$ SST model, (b) Comparing X-Velocity predictions to experimental data, (c) Upper surface of diffuser, (d) Lower surface of diffuser.

model-form uncertainty present in this problem, motivating our investigation into a method that accounts for this uncertainty in design optimization.

3. Optimization Setup

With our computational setup, initially we perform deterministic optimization studies on the diffuser shape using our automated grid generation and the design parameters given in Table I.

Design Parameter	Lower Bound	Upper Bound	Baseline Value
Diffuser Length	$10h$	$30h$	$22.7h$
Outlet Channel Width	$2h$	$15h$	$4.7h$
Ramp Corner Radius	$3h$	$13h$	$9.7h$
FFD Control Point 1	$-2h$	$2h$	$0h$
FFD Control Point 2	$-2h$	$2h$	$0h$
FFD Control Point 3	$-2h$	$2h$	$0h$
FFD Control Point 4	$-2h$	$2h$	$0h$
FFD Control Point 5	$-2h$	$2h$	$0h$

TABLE I: Design Parameters

The free-form deformation (FFD) control points form a 8^{th} order spline, with 9 evenly spaced control points along the ramp length. The inner 5 FFD control points can move vertically to deform the shape of the ramp. This keeps the inlet and outlet widths unaffected by the FFD deformation, letting the FFD points only deform the ramp itself.

The objective function to be minimized is the pressure recovery (given by equation 7) between the inlet plane and a plane 30 channel widths downstream of the diffuser. The derivative-free optimizer COBYLA (Constrained Optimization By Linear Approximation)³¹ is used. The COBYLA algorithm forms a linear approximation of the objective and constraints using interpolation of the vertices of a simplex, and a trust region to bound the changes to variables at each iteration.

4. Deterministic optimization

To investigate how deterministic design optimization using turbulence models can lead to designs that depend upon the choice of turbulence model, here we consider two separate diffuser design cases.

The first case considered is when the length of the diffuser is fixed at $22.7h$, and the width is

fixed at $4.7h$, and we run two optimization studies, one using the SA model and one using the SST model. In Figure 5, the convergence of the two optimizations are given. The figure reports the history of the objective function (normalized pressure recovery, on the y -axis) at successive design optimization iterations, reported on the x -axis. Every design optimization iteration represents an intermediate design in the evolution of the diffuser design from the initial to the optimal design.

On Figure 6, the resulting diffuser shapes and skin friction distributions along the lower surface are plotted. Additionally, results from Lim and Choi¹¹ are given for this case, where the more advanced $k-\epsilon-v^2-f$ turbulence model is used. As can be seen, the final optimized design is sensitive to the choice of the turbulence model. Additionally, the performance of the optimal design varies substantially, depending upon the turbulence model utilized.

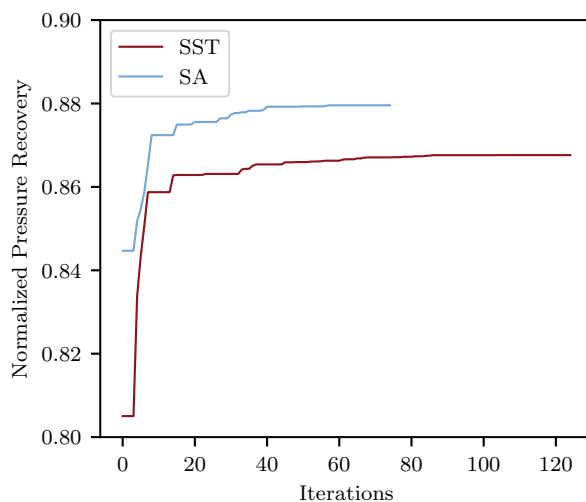


FIG. 5: Convergence of optimizations, for $L = 22.7h$ and $W = 4.7h$.

We can see that the same qualitative shape has been obtained in all three cases: a bump in the ramp surface with an initial rapid expansion over the diffuser throat, such that the flow stays attached until the end of the bump. This is most extreme in the optimal deterministic design of Lim and Choi¹¹, but this can be explained by a comparison between the $k-\epsilon-v^2-f$ and SST turbulence models conducted in Lim and Choi¹¹: the SST predicts separation earlier than the $k-\epsilon-v^2-f$ model. Therefore the more rapid expansion after the diffuser throat for the optimal design of Lim and Choi¹¹ would likely cause the SST model to separate earlier. From the validation results in Figure 4d, we can see that the SA model predicts separation later than the SST model on the baseline geometry, which explains why the optimal design using the SA model is between the SST and $k-\epsilon-v^2-f$ optimal designs.

Optimization under turbulence model uncertainty for aerospace design

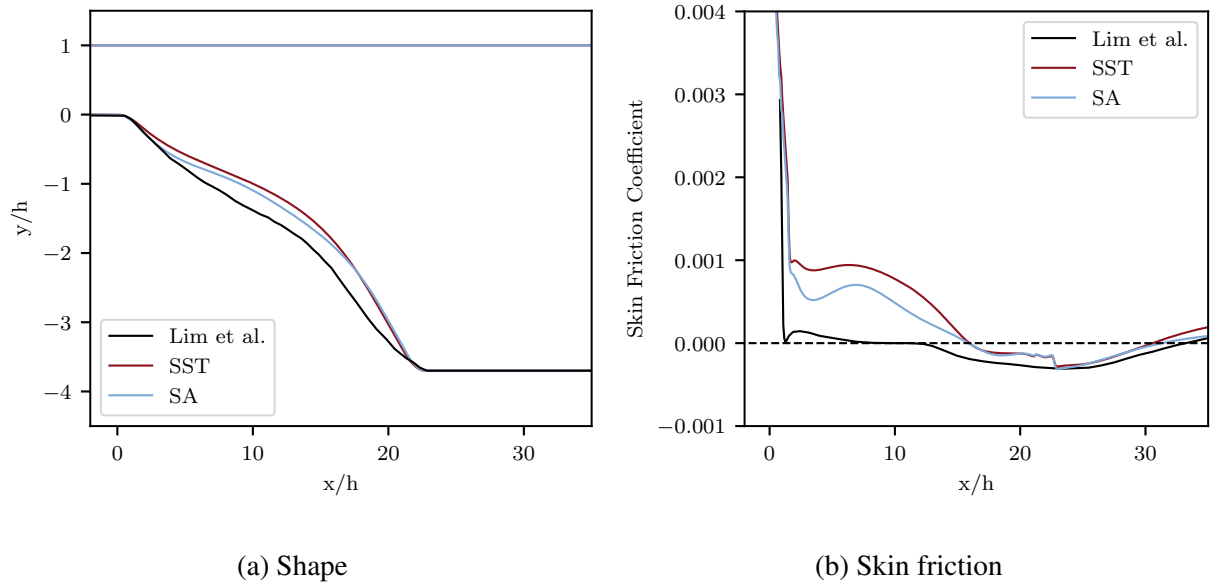


FIG. 6: (a) Diffuser shape and (b) skin friction coefficient for the optimal designs.

The second case considered is when the length of the diffuser is fixed at $22.7h$, and the width is free to vary. On Figure 7, the convergence of the two optimizations are given, and on Figure 8, the resulting diffuser shapes and skin friction distributions along the lower surface are plotted. Once again, we observe that the optimized design and the optimal performance of the diffuser for this case are sensitive to the choice of the turbulence model used. This sensitivity indicates that the optimization is sensitive to the uncertainties and error in individual turbulence models as well.

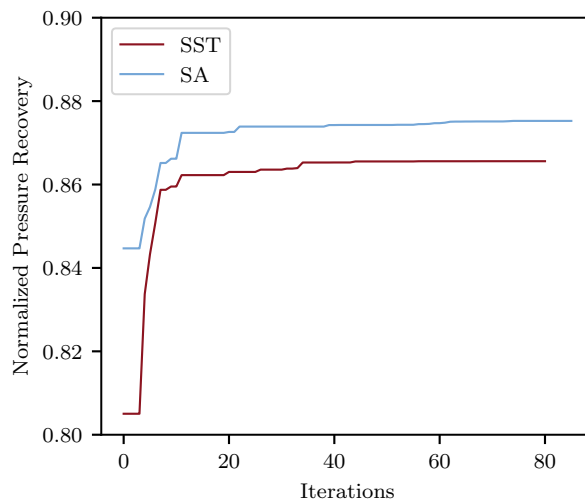


FIG. 7: Convergence of optimizations, for $L = 22.7h$ and $W = \text{free}$.

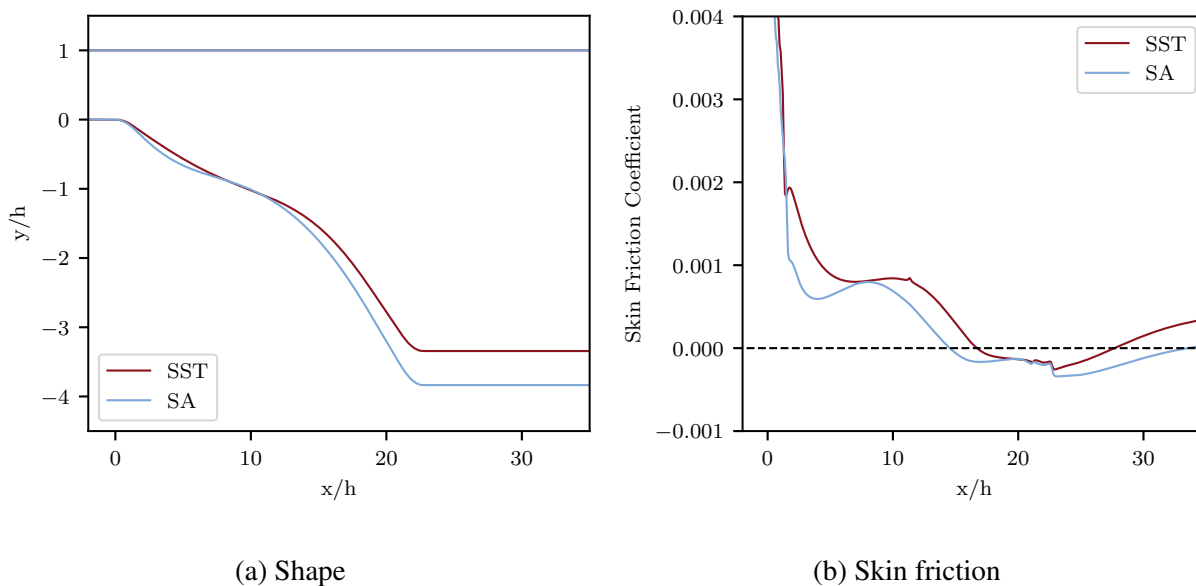


FIG. 8: (a)Diffuser shape and (b)skin friction coefficient for the optimal designs.

Using optimization for design problems such as this means that if the number of design parameters were increased, the optimum designs may vary slightly. Here, based on the difference in shapes of the different optimization cases, our parameterization scheme is sufficient to capture key physical differences and so is sufficient for the purposes of this investigatory study. In a real design optimization, more optimization parameters may be used to slightly improve the design at the cost of increased computational effort.

5. Optimization under uncertainty

Next we carry out optimization studies using the eigenspace perturbation methodology to design the diffuser for similar cases as investigated in for deterministic design optimization. To illustrate the enveloping approach, figure 9 gives the predicted skin friction coefficient at the lower surface of the diffuser for the nominal SST model and the 5 perturbed RANS simulations, for the baseline diffuser (length= $22.7h$) and a longer diffuser (length= $40h$).

Next, we optimize the long diffuser using both the deterministic SST model, as well as our optimization under uncertainty approach where we optimize for the worst case of the objective function over the eigenspace perturbation solutions. The convergence of the deterministic optimization is reported in Figure 10, and the optimal diffuser shapes and predicted skin friction are

Optimization under turbulence model uncertainty for aerospace design

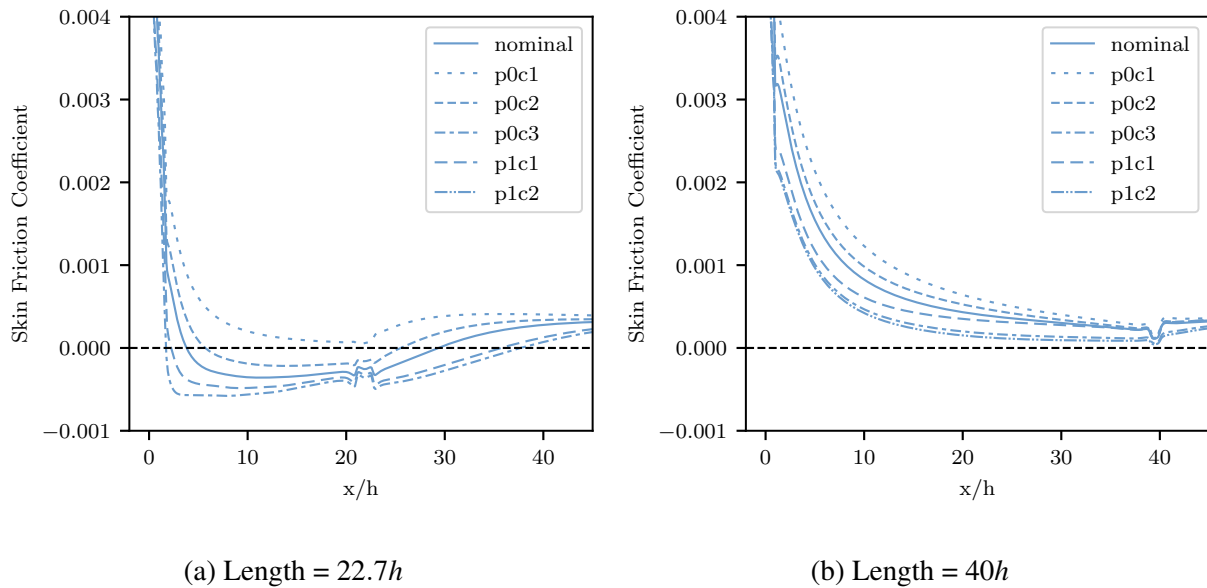


FIG. 9: Predicted skin friction coefficient at the lower surface of the diffuser for the nominal turbulence model and the perturbed RANS simulations: (a)Length = $22.7h$, (b)Length = $40h$

plotted on Figure 11, where they are compared with the baseline long diffuser.

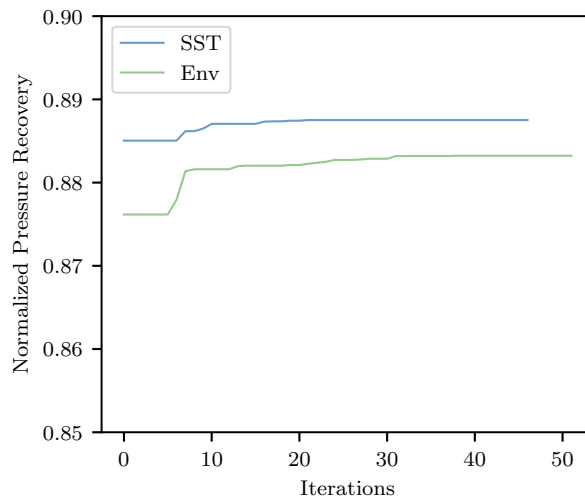


FIG. 10: Convergence of the optimizations

It is clear that the enveloping optimum is different to the deterministic optimum. Both designs exhibit a bump on the ramped surface, but the enveloping optimum delays the end of this bump to farther downstream.

The improvement in robustness of the optimized design with respect to turbulence uncertainty

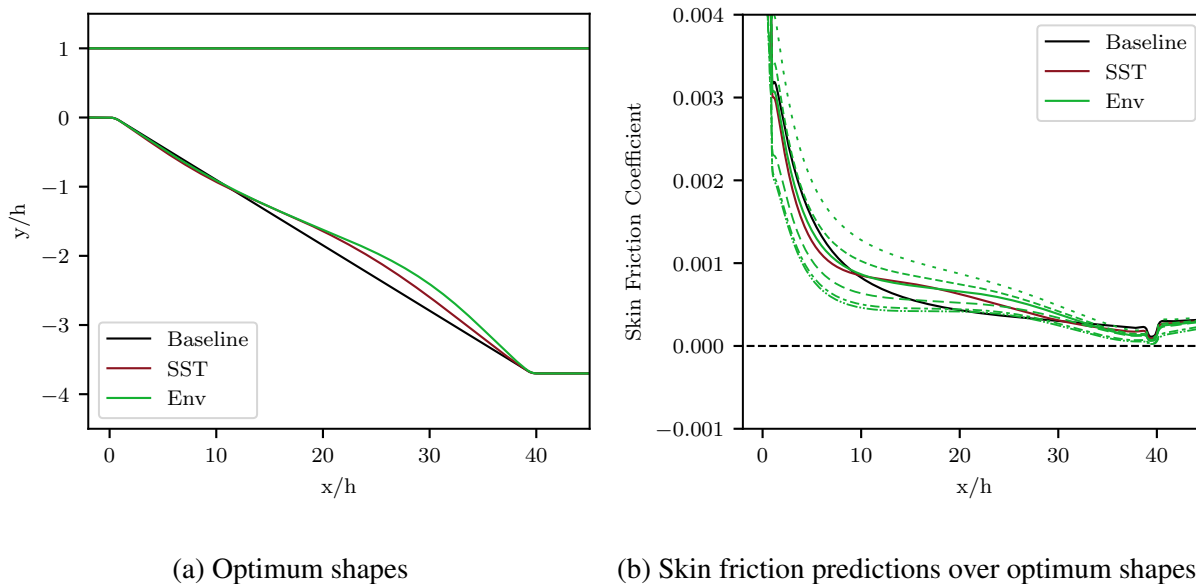


FIG. 11: Optimization Results: (a)Optimum shapes, (b)Skin friction predictions over optimum shapes

can be understood physically by considering the physics based rationale of the objective function used during optimization, along with the nature of the uncertainty exhibited by the SST model. The objective function used in the optimization is pressure recovery, defined in equation 7. The primary objective of any diffuser is to recover the static pressure via reduction of the flow velocity. Ideally, a diffuser design should be able to convert the maximum possible kinetic energy to pressure. Pressure recovery measures the rise in static pressure of the flow as it passes through the design. However, the adverse pressure gradients along the expansion section of the diffuser lead thicker boundary layers on the lower surface in the expansion section. Such thicker boundary layers are more susceptible to flow separation. If such flow separation occurs and a reverse flow region is formed, the effective flow area shrinks. This causes the mean streamwise velocity to increase. As a result, the pressure recovery of the diffuser is degraded. This flow separation results in total pressure loss, causing lower static pressure rise and thus degrading pressure recovery. Thus, the key parameter to maximize pressure recovery across the diffuser is to ensure mitigation of flow separation.

In spite of the superior accuracy of the SST model (as compared to the SA model, for instance), the SST model predictions exhibit discrepancy in the C_f prediction on the lower surface of the diffuser, where the flow separation and re-attachment manifests. In this context, it has been exhibited

that RANS based models underpredict the length of the diffuser separation bubble by over 10%³². This is exhibited in Figure 12. Figure 12 (a) and (c) report the mean streamlines in the diffuser for the extremal perturbations, compared to the case for the nominal, unperturbed turbulence model in (b). As can be seen, the extent of the separation bubble can be larger than that predicted by the nominal, unperturbed turbulence model. This degrades the robustness of designs optimized using the baseline RANS model. Even at such an optimized deterministic design, where the flow separation is (say) absent according to the nominal turbulence model, the real flow may still exhibit separation thus degrading pressure recovery. As is reported in Figure 11, the OUU optimized design ensures that not only is flow separation suppressed completely for the nominal turbulence model, it is also absent in the perturbed RANS predictions. This ensures that the diffuser pressure recovery is optimized, and the design is robust to the errors and uncertainties of the RANS model.

This highlights how using the enveloping method within our optimization framework resulted in a design that is less sensitive to the turbulence-modelling uncertainties inherent in the simulation.

B. NACA0012 airfoil at high angle of attack

Airfoil shapes form an important component for the design and performance of various aerospace applications, such as the wing tips of aircraft, inboard and outboard blades of helicopters, along with wind turbine blades. The performance of these applications can benefit from careful airfoil shape optimization. Deterministic optimization of airfoil shapes often leads to designs where the actual performance is substantially worse than in simulations due to uncertainties in simulations^{33,34}.

A significant measure of this uncertainty can be attributed to the turbulence models used in simulations. This is exhibited in figure 13, where the variation in the coefficient of lift, C_L , with the angle of attack, α , is reported for the NACA 0012 and NACA 4412 shapes. The experimental data are represented by filled circles and correspond to the experiment of Ladson³⁵ for the NACA 0012 airfoil and Coles and Wadcock³⁶ for the NACA 4412 airfoil case. The baseline $k - \omega$ SST model predictions by the dark line. As can be observed in the figure, at low angles of attack, the predictions of the RANS model agree with the experimental data. However, the fidelity of the RANS model deteriorates at higher angles of attack. For instance, at higher angles of attack closer to stall for the NACA 0012 airfoil case, the RANS model predicts stall at an angle of attack of

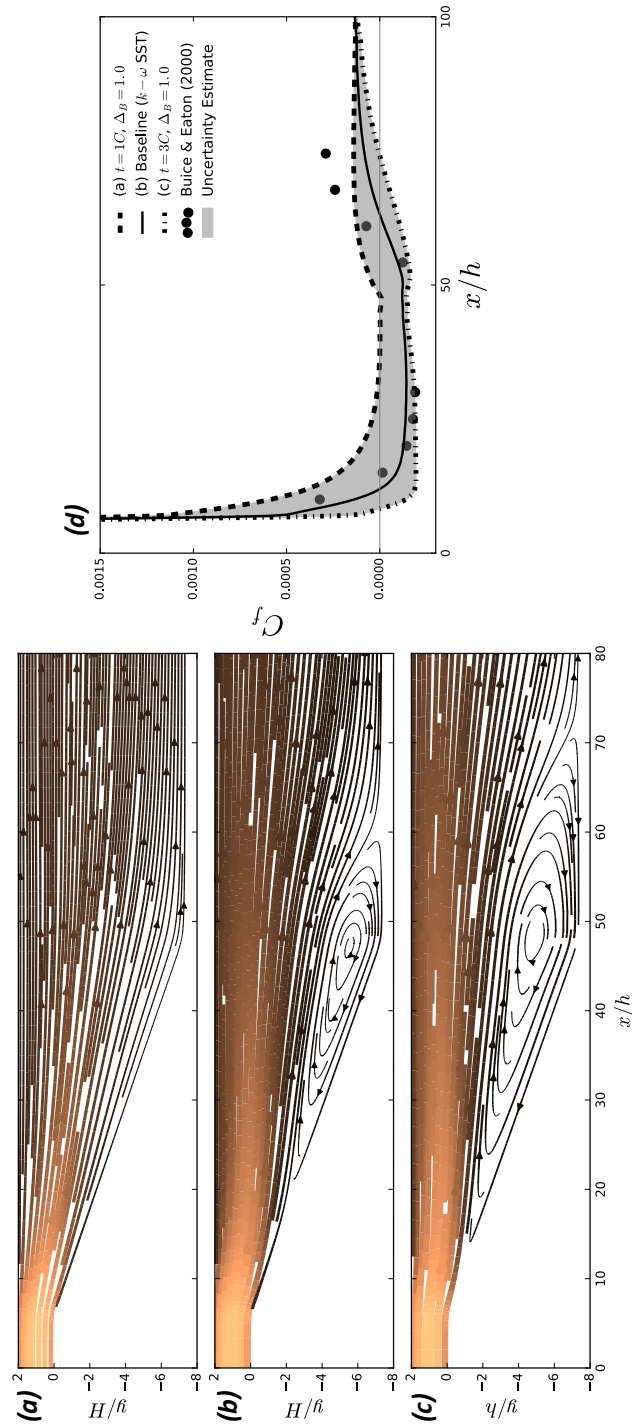


FIG. 12: Modeling rationale for Design Under Uncertainty (DUU) design: (a) Diffuser mean streamlines under maximal production perturbation, (b) Mean streamlines predicted by unperturbed model, (c) Diffuser mean streamlines under minimal production perturbation, (d) Coefficient of friction over the lower surface of the diffuser.

12°. The experimental data suggest that this phenomenon occurs at an angle of attack of 18°. On the contrary, for the NACA 4412 airfoil case, the RANS model under-predicts the incidence and severity of stall. Thus, a major source of uncertainty in airfoil design and optimization are the RANS models used in simulations. It has been observed in prior literature that the optimized airfoil shape is highly sensitive to the choice of the RANS model used in design simulations¹⁰.

For both the airfoil shapes, the uncertainty estimates for C_L given by the eigenspace perturbation methodology are exhibited in figure 13 via the grey shaded zone. The figures reflect that the eigenspace perturbation methodology is able to account for the discrepancy between RANS predictions and high fidelity data.

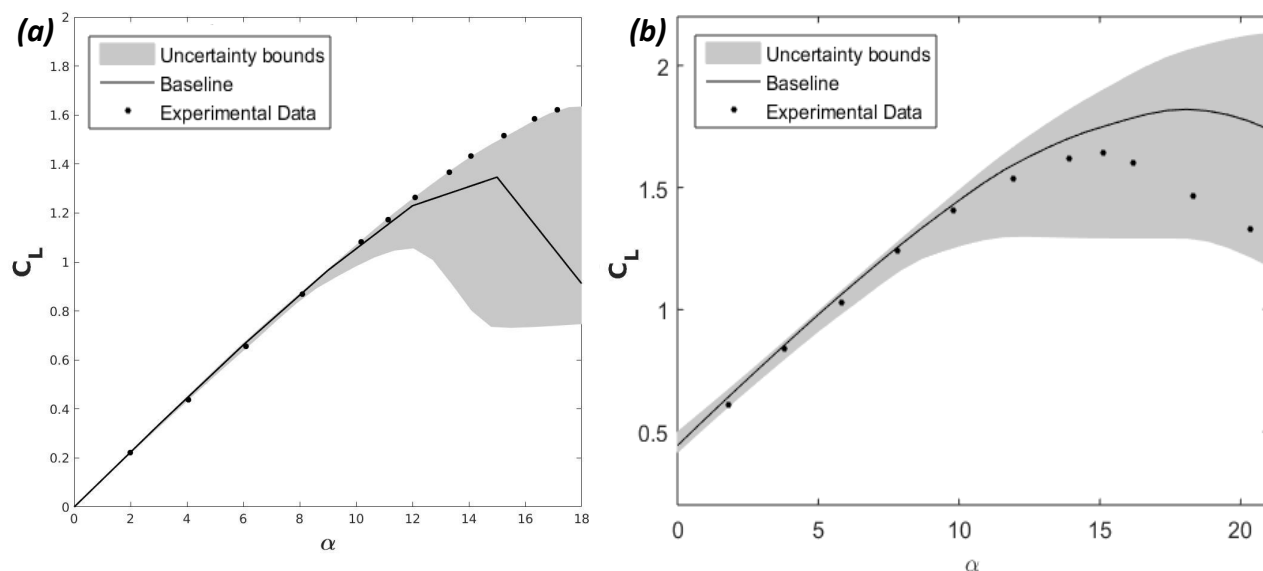


FIG. 13: Variation in the coefficient of lift, C_L , with the angle of attack, α , for the (a) NACA 0012 airfoil with the experimental data of Ladson³⁵, (b) NACA 4412 airfoil with the experimental data of Coles and Wadcock³⁶.

1. Computational Setup

Here, we outline the conditions for the NACA 4412 experiment of Coles and Wadcock³⁶. Thence, the computational domain and setup and the numerical schemes for our simulations in figure 13 (b) are outlined. The same discussions for the NACA 0012 airfoil simulations and the experiment of Ladson³⁵ are discussed afterwards.

The NACA 4412 airfoil experiment corresponds to free-stream conditions of $M = 0.09$, $Re_c =$

1.52×10^6 and $T = 300K$. The two-dimensional discretized domain consists of an unstructured, O-mesh conforming to the airfoil surface with 36,145 total elements. The mesh is hybrid with quadrilaterals in the regions adjacent to the airfoil surface and triangular elements in the remaining domain. The far field boundary is over 20 chord lengths away from the airfoil. The mesh spacing at the airfoil surface is small enough to ensure $y^+ < 1$ and the mesh independence has been reported³⁷. With respect to the numerical scheme, we utilize Roe’s second order upwind scheme³⁸ to calculate the convective fluxes and use the Venkatakrisnan’s limiter³⁹ on the primitive variables. Turbulent variables are convected using a second order scalar upwind method and the viscous fluxes are calculated using the corrected average gradient method. Implicit time stepping is utilized to converge to the steady state solution and the linear system is solved with the Generalized Minimal Residual method⁴⁰ with a maximum error tolerance of $0(10^{-6})$.

The NACA 0012 airfoil experiment corresponds to free-stream conditions of $M = 0.15$, $Re_c = 6 \times 10^6$ and $T = 300K$. The two-dimensional discretized domain consists of a C-mesh of quadrilateral elements conforming to the airfoil surface with 897 nodes in the airfoil-normal and 257 nodes in the airfoil-tangent directions. The far field boundary is placed over 500 chord lengths from the airfoil surface. The mesh spacing at the airfoil surface is small enough to ensure $y^+ < 1$ and the mesh independence has been reported³⁷. We utilize Roe’s second order upwind scheme³⁸ to calculate the convective fluxes and use the Venkatakrisnan’s limiter³⁹ on the primitive variables. The turbulent variables for the closure models are convected using a first-order scalar upwind method. The viscous fluxes are calculated using the corrected average gradient method. Implicit time stepping is utilized to converge to the steady state solution and the linear system is solved with the Generalized Minimal Residual method⁴⁰ with a maximum error tolerance of $0(10^{-6})$ for the nonlinear iterations of the flow solver.

2. Optimization Setup

In light of the behaviour illustrated on Figure 13, the design of a NACA 0012 airfoil near stall is chosen as a test problem for design under turbulence model form uncertainty. For this investigation, we perform optimizations at a single angle of attack, 14° .

The objective is to minimize $-1 \times$ lift to drag ratio, at a Mach number of 0.15 and a Reynolds number of 6×10^6 , starting from the baseline NACA0012 geometry. The design space is parameterized using 4 Hicks-Henne bump functions on the upper and lower surfaces of the airfoil,

located at the following chord locations: 0.2, 0.4, 0.6, 0.8. The bounds on these design variables are ± 0.05 chord lengths. Hicks-Henne bump functions (in contrast to free form deformation) deform the surface by super-imposing a bump function (with zero derivative at either end to ensure smooth deformation) of variable magnitude on the airfoil geometry at a given location; it is a common method of parameterizing airfoil shapes for optimization⁴¹.

A geometry constraint is imposed: a torsion box of size 0.5×0.08 chord lengths (that just fits inside the NACA0012, as exhibited in figure 14) airfoil must fit inside the deformed geometry. This is measured by “box protrusion” which must be ≤ 0 .

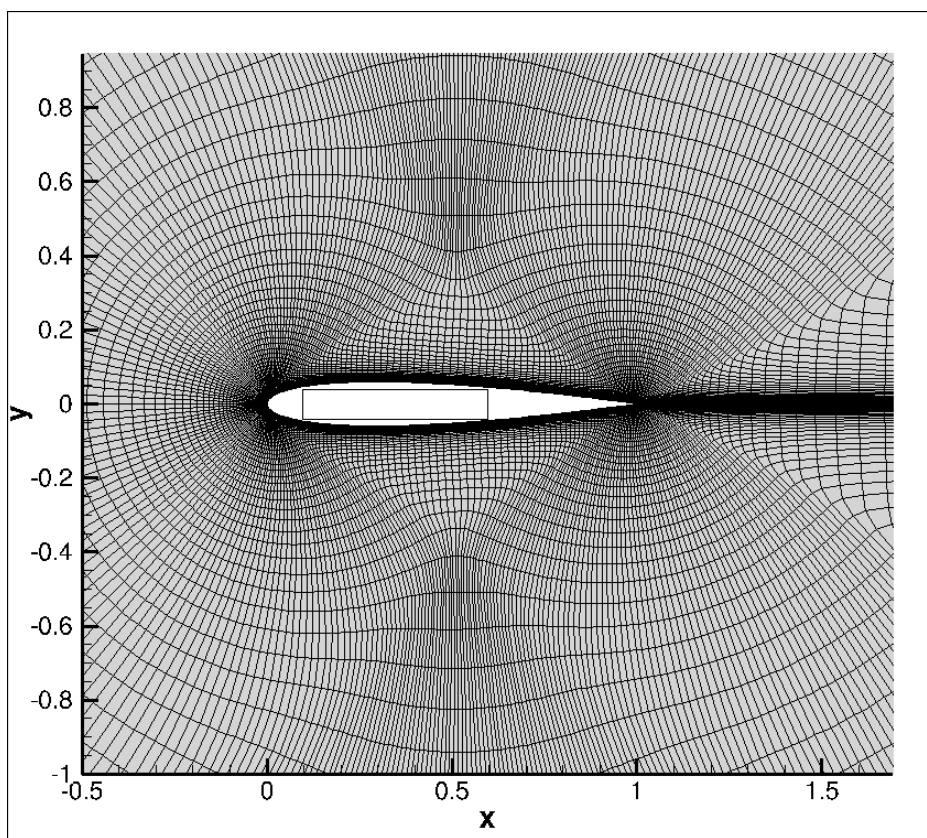


FIG. 14: Mesh and box for the baseline NACA0012 airfoil

Since it is not trivial to obtain a gradient for the worst-case L/D , here we use the derivative free optimizer COBYLA³¹ to avoid any issues with gradient analysis. We run a deterministic optimization, where no eigenspace perturbations are performed, and an “enveloping” optimization, where the worst case over the five enveloping simulations is optimized. This worst case L/D is found using interval arithmetic on the values of lift and drag.

3. Optimization Results

The following labels are used: “Det” refers to the optimization minimizing $-L/D$, “Env” refers to the optimization minimizing the worst case of $-L/D$ over the five enveloping runs, “Nominal” refers to a simulation without any eigenspace perturbations, and “n0012” refers to the NACA0012 airfoil. Figure 15 gives the convergence of the optimizations, as well as the airfoil shapes of the designs resulting from each optimization.

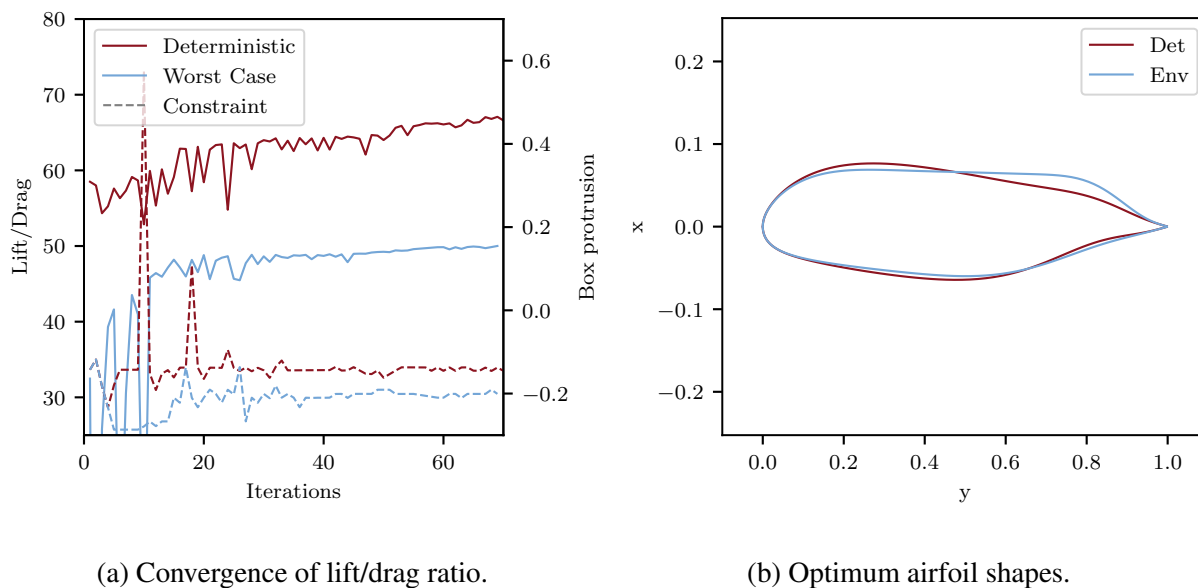


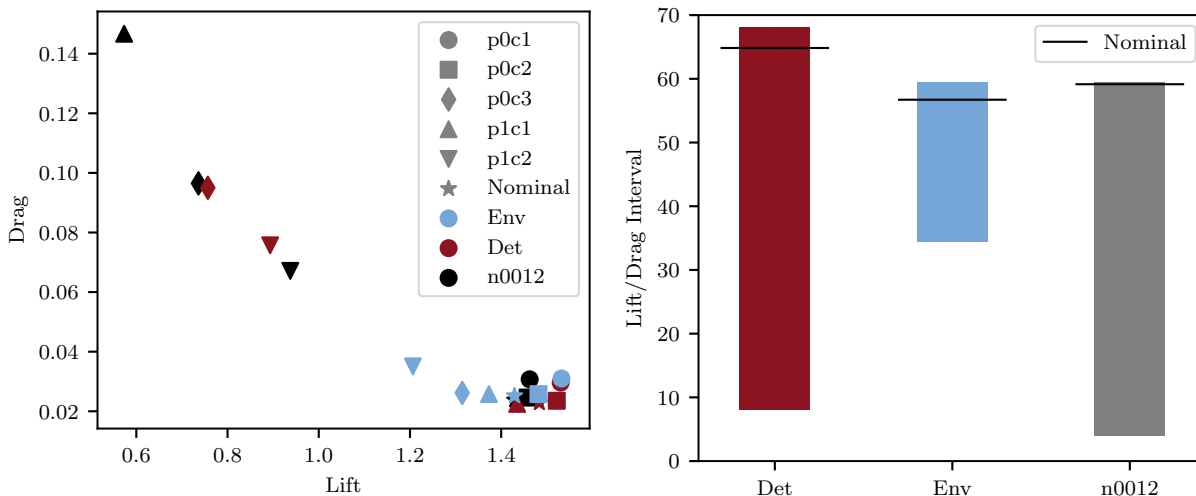
FIG. 15: Optimization results: (a) Convergence history given as the lift/drag ratio at each optimization iteration, (b) Optimum airfoil shapes.

The differences in the shapes of the two optimized airfoils can be analyzed considering the flow physics, the underlying model predictions and the optimization objective function. Maximizing the ratio of lift to drag is a common objective in the optimization of airfoils. Here, the drag over the airfoil is composed of the friction drag (due to viscous shear), and form drag (due to displacements of boundary layers and the ensuing wake). At high Reynolds numbers and with separation, the form drag and the ensuing airfoil performance is heavily influenced by the separation bubble, located at the onset of the pressure recovery region. While both the size and the location of this separation bubble are functions of the airfoil shape, the angle of attack, etc, the size of the bubble is the key parameter to maximize the objective function. If the separation bubble is small, the mixing losses can be minimized. However, if the bubble is large, the ensuing mixing lead to large increment in the drag.

During optimization, the degrees of freedom on the shape of the airfoil are used to create the characteristic bump on the airfoil, to fill the space of the potential separation bubble^{42,43}. This peculiarity of the shape reduces the drag occurring due to the mixing during the separation and re-attachment.

For the optimization at 14° , the baseline SST $k - \omega$ model predicts mild separation. Under such conditions, adding a bump to the profile would not alleviate the form drag significantly, while it would increase friction drag. However, for the optimization under uncertainty, we are optimizing for a case under severe separation. Thus, for the latter case, the optimization leads to the manifestation of the pronounced characteristic bump on the suction surface of the airfoil to minimize the form drag.

To further investigate these two designs, the lift and drag values resulting from the five enveloping simulations are plotted on Figure 16, where they are compared to the baseline NACA0012 design. On Figure 17, the upper surface pressure and friction distributions evaluated by each enveloping simulation are plotted for the optimum airfoils. On Figure 18, the lift and drag polars of the optimum designs are plotted.



(a) Lift and drag of enveloping simulations

(b) Nominal value and bounds on lift-to-drag

FIG. 16: Forces for perturbed simulations on the two optimum airfoils. (a) Lift and drag of enveloping simulations, (b) Nominal value and bounds on lift-to-drag

Optimization under turbulence model uncertainty for aerospace design

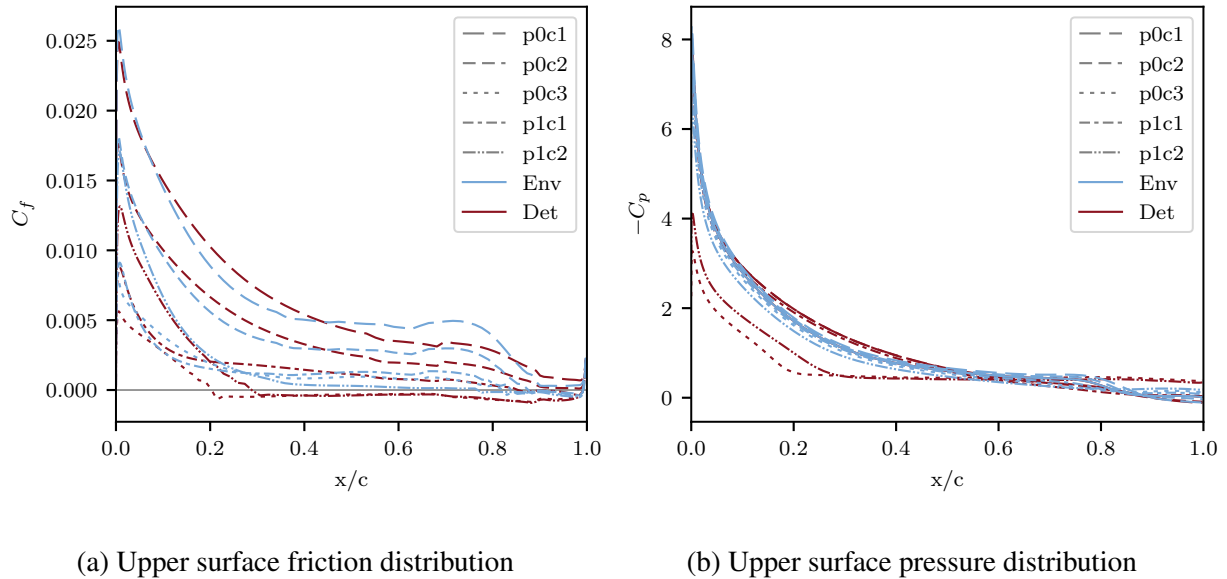


FIG. 17: Friction and pressure distributions over the upper surface of the two optimum airfoils.

"Env" indicates the design resulting from optimization of the worst case from the perturbed simulations, and "det" indicates that resulting from deterministic optimization. (a) Upper surface friction distribution, (b) Upper surface pressure distribution.

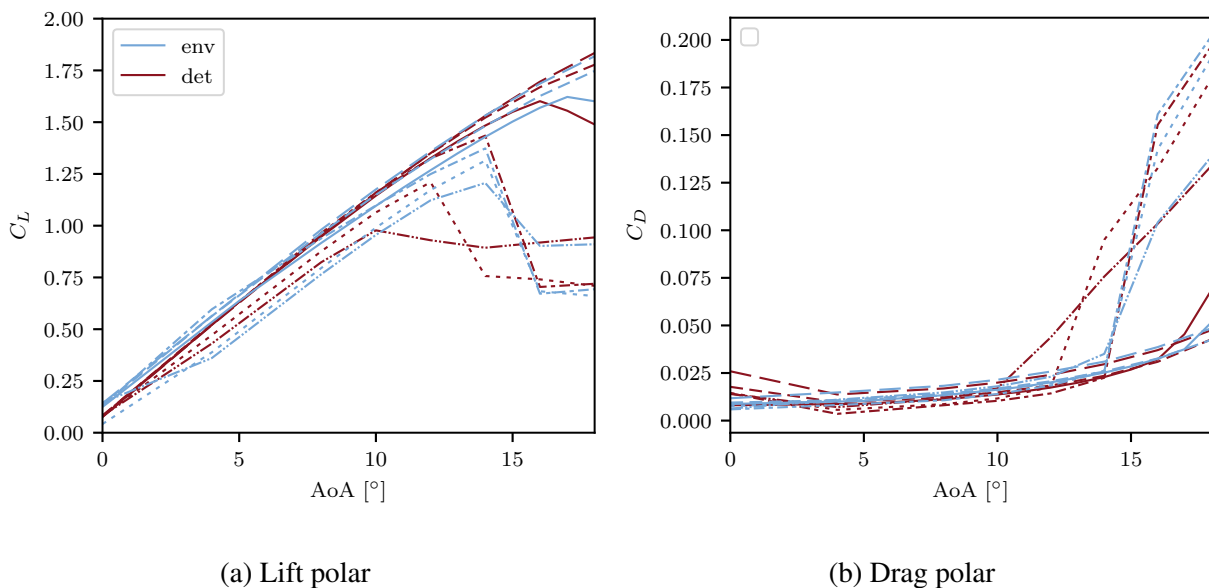


FIG. 18: Polars of deterministic optimum airfoil. "Env" indicates the design resulting from optimization of the worst case from the perturbed simulations, and "det" indicates that resulting from deterministic optimization. (a) Lift Polar, (b) Drag Polar.

These results show a clear difference between the optimal designs resulting from a deterministic optimization and the enveloping approach. The deterministic optimum begins to stall in a perturbed solution on Figure 18 as early as 10° , whereas no solution begins to stall until 14° for the enveloping optimum. This indicates a design that is more robust with respect to turbulence-based modelling uncertainties.

We can also see from figure 16 that the drop off in performance under multiple of the perturbed solutions is significant (the solutions in the upper left of figure 16a). Therefore this improved robustness is desired from a design point of view.

We can observe that due to there being a reasonably linear correlation between increased lift and reduced drag in the variation in the perturbed solutions on Figure 16a, the reduction in performance is primarily due to earlier separation.

IV. CONCLUSIONS

Turbulence models have structural uncertainties associated with their predictions. When turbulence models are used in design optimization, they can lead to sub-optimal designs whose performance is degraded in reality compared to the predicted performance. Numerous investigators have observed that designs optimized using a given turbulence model are sensitive to the choice of the turbulence model. While the importance of accounting for turbulence model-form uncertainty in design optimization has been established, not much research has been done to this end.

In this investigation, we outline a design under uncertainty methodology intended to obtain an optimized design that is robust to the structural uncertainty in turbulence models. This is done via the use of an optimization under uncertainty (OUU) formulation in conjunction with the eigenspace perturbation uncertainty estimation framework.

In both an asymmetric diffuser and an airfoil design problem, we find that the designs resulting from our OUU formulation exhibit higher robustness to turbulence model form uncertainty. Additionally, using numerical experiments over different turbulence models, we illustrate how deterministic design optimization using turbulence models leads to designs that are not universal but are dependent upon the choice of the turbulence model.

This study is a first step towards answering the question of how turbulence modelling uncertainty should most appropriately be considered in a simulation-based design framework. When probabilistic operational uncertainties are also present, the problem becomes a mixed-uncertainty

optimization problem, for which recently developed OUU methods may be well suited.

REFERENCES

- ¹A. Keane, “Computational approaches for aerospace design: The pursuit of excellence,” (Wiley, New York, 2005).
- ²M. Kennedy and A. O’Hagan, “Bayesian calibration of computer models,” *Journal of the Royal Statistical Society, Series B (Statistical Methodology)* **63** (2001).
- ³H. Beyer and B. Sendhoff, “Robust optimization - a comprehensive survey,” *Computer Methods in Applied Mechanics and Engineering* **196** (2007).
- ⁴B. Launder, D. Tselepidakis, and B. Younis, “A second-moment closure study of rotating channel flow,” *Journal of Fluid Mechanics* **183**, 63–75 (1987).
- ⁵T. Craft, B. Launder, and K. Suga, “Development and application of a cubic eddy-viscosity model of turbulence,” *International Journal of Heat and Fluid Flow* **17**, 108–115 (1996), doi: 10.1016/0142-727X(95)00079-6.
- ⁶H. Steiner, S. Jakirlic, G. Kadavelil, S. Saric, R. Manceau, and G. Brenn, “Report on 13th ERCOFTAC workshop on refined turbulence modelling,” *ERCOFTAC Bulletin* , 24–29 (2009).
- ⁷S. Jakirlic, G. Kadavelil, E. Sirbubalo, D. von Terzi, M. Breuer, and D. Borello, “14th ERCOFTAC SIG15 workshop on turbulence modelling: Turbulent flow separation in a 3-d diffuser,” *ERCOFTAC Bulletin* , 5–13 (2010).
- ⁸G. Mompean, S. Gavrilakis, L. Machiels, and M. Deville, “On predicting the turbulence-induced secondary flows using nonlinear k- ϵ models,” *Physics of Fluids* **8**, 1856–1868 (1996), doi: 10.1063/1.868968.
- ⁹A. Vuruskan and S. Hosder, “Impact of turbulence models and shape parameterization on robust aerodynamic shape optimization,” *Journal of Aircraft* , 1–17 (2018).
- ¹⁰T. D. Ivanov, A. M. Simonović, N. Petrović, V. G. Fotev, and I. A. Kostić, “Influence of selected turbulence model on the optimization of a class-shape transformation parameterized airfoil.” *Thermal Science* **21** (2017).
- ¹¹S. Lim and H. Choi, “Optimal shape design of a two-dimensional asymmetric diffuser in turbulent flow,” *AIAA journal* **42**, 1154–1169 (2004).
- ¹²A. Vuruskan and S. Hosder, “Investigation of the impact of turbulence models on robust aerodynamic shape optimization,” in *2018 AIAA Aerospace Sciences Meeting* (2018) p. 0553.

- ¹³A. A. Mishra, J. Mukhopadhaya, G. Iaccarino, and J. Alonso, “Uncertainty estimation module for turbulence model predictions in SU2,” *AIAA Journal* **57**, 1066–1077 (2018).
- ¹⁴G. Iaccarino, A. Mishra, and S. Ghili, “Eigenspace perturbations for uncertainty estimation of single-point turbulence closures,” *Physical Review Fluids* **2** (2017), doi: 10.1103/PhysRevFluids.2.024605.
- ¹⁵S. Banerjee, R. Krahl, F. Durst, and C. Zenger, “Presentation of anisotropy properties of turbulence, invariants versus eigenvalue approaches,” *Journal of Turbulence* **8**, N32 (2007), doi: 10.1080/14685240701506896.
- ¹⁶C. Buice and J. Eaton, “Experimental investigation of flow through an asymmetric plane diffuser, dept. of mech. eng,” (1997).
- ¹⁷M. M. Putko, A. C. Taylor, P. A. Newman, and L. L. Green, “Approach for input uncertainty propagation and robust design in CFD using sensitivity derivatives,” *Journal of Fluids Engineering* **124**, 60–69 (2002).
- ¹⁸M. E. Harr, *Reliability based design* (Dover, New York, 1996).
- ¹⁹L. Cook and J. Jarret, “Optimization using multiple dominance criteria for aerospace design under uncertainty,” *AIAA Journal* **56** (2018).
- ²⁰D. Bertsimas and M. Sim, “The price of robustness,” *Operations research* **52**, 35–53 (2004).
- ²¹A. H. Shokouhi, A. Hatami-Marbini, M. Tavana, and S. Saati, “A robust optimization approach for imprecise data envelopment analysis,” *Computers & Industrial Engineering* **59**, 387–397 (2010).
- ²²A. Ben-tal and A. Nemirovski, “Robust convex optimization,” *Mathematics of Operations Research* **23** (1998).
- ²³“Comparison of robust optimization methods applied to hypersonic vehicle design,” *Journal of Aircraft* **52** (2015).
- ²⁴F. R. Menter, “Two-equation eddy-viscosity turbulence models for engineering applications,” *AIAA journal* **32**, 1598–1605 (1994).
- ²⁵P. Spalart and S. Allmaras, “A one-equation turbulence model for aerodynamic flows,” in *30th aerospace sciences meeting and exhibit* (1992) p. 439.
- ²⁶E. M. Cherry, C. J. Elkins, and J. K. Eaton, “Geometric sensitivity of three-dimensional separated flows,” *International Journal of Heat and Fluid Flow* **29**, 803–811 (2008).
- ²⁷E. Cherry, G. Iaccarino, C. Elkins, and J. Eaton, “Separated flow in a three-dimensional diffuser: preliminary validation,” *Annual Research Briefs* **2006**, 57–83 (2006).

- ²⁸D. G. Wilson and T. Korakianitis, *The design of high-efficiency turbomachinery and gas turbines* (MIT press, 2014).
- ²⁹T. W. Sederberg and S. R. Parry, “Free-form deformation of solid geometric models,” *SIGGRAPH Computer Graphics* **20** (1986).
- ³⁰S. Obi, K. Aoki, and S. Masuda, “Experimental and computational study of turbulent separating flow in an asymmetric plane diffuser,” in *Ninth Symposium on Turbulent Shear Flows, Hyoto, Japan* (1993).
- ³¹M. J. Powell, “A direct search optimization method that models the objective and constraint functions by linear interpolation,” in *Advances in optimization and numerical analysis* (Springer, 1994) pp. 51–67.
- ³²C. Heschl, K. Inthavong, W. Sanz, and J. Tu, “Evaluation and improvements of rans turbulence models for linear diffuser flows,” *Computers & fluids* **71**, 272–282 (2013).
- ³³M. Drela, “Pros and cons of airfoil optimization,” *Frontiers of computational fluid dynamics* **1998**, 363–381 (1998).
- ³⁴L. Huyse, S. L. Padula, R. M. Lewis, and W. Li, “Probabilistic approach to free-form airfoil shape optimization under uncertainty,” *AIAA journal* **40**, 1764–1772 (2002).
- ³⁵C. Ladson, “Effects of independent variation of mach and reynolds numbers on the low-speed aerodynamic characteristics of the naca 0012 airfoil section nasa-tm-4074,(l-16472, nas 1.15: 4074),” Hampton, VA: National Aeronautics and Space Administration, Langley Research Center (1988).
- ³⁶D. Coles and A. J. Wadcock, “Flying-hot-wire study of flow past an naca 4412 airfoil at maximum lift,” *AIAA Journal* **17**, 321–329 (1979).
- ³⁷F. Palacios, T. D. Economou, A. C. Aranake, S. R. Copeland, A. K. Lonkar, T. W. Lukaczyk, D. E. Manosalvas, K. R. Naik, A. S. Padrón, B. Tracey, *et al.*, “Stanford university unstructured (su2): Open-source analysis and design technology for turbulent flows,” *AIAA paper* **243**, 13–17 (2014).
- ³⁸P. L. Roe, “Approximate riemann solvers, parameter vectors, and difference schemes,” *Journal of computational physics* **43**, 357–372 (1981).
- ³⁹V. Venkatakrishnan, “Convergence to steady state solutions of the euler equations on unstructured grids with limiters,” *Journal of computational physics* **118**, 120–130 (1995).
- ⁴⁰Y. Saad and M. H. Schultz, “Gmres: A generalized minimal residual algorithm for solving nonsymmetric linear systems,” *SIAM Journal on scientific and statistical computing* **7**, 856–869

(1986).

⁴¹.

⁴²M. Drela, “Low-reynolds-number airfoil design for the mit daedalus prototype-a case study,” *Journal of Aircraft* **25**, 724–732 (1988).

⁴³L. Huyse, “Free-form airfoil shape optimization under uncertainty using maximum expected value and second-order second-moment strategies,” Tech. Rep. NASA/CR-2001-21102 (Hampton, Virginia, 2001).